PERGAMON

International Journal of Solids and Structures 40 (2003) 5455–5475

INTERNATIONAL JOURNAL OF SOLIDS and STRUCTURES

www.elsevier.com/locate/ijsolstr

Experiments on the penetration of thin long-rod projectiles into thick long-cylindrical borosilicate targets under pressure-free polycarbonate, aluminum and steel confinements

Mulalo Doyoyo *

Impact and Crashworthiness Laboratory, Massachusetts Institute of Technology, 77 Massachusetts Avenue, Cambridge, MA 02139-4307, USA

Received 13 June 2002; received in revised form 9 April 2003

Abstract

It is well established that confinement pressure inhibits comminution and fragment-flow during projectile penetration of ceramics. Here, a high-pressure gas gun is used to investigate the role of confinement wave impedance on the failure kinetics of ceramics during penetration. Tool-steel rods of fixed lengths and L/D ratios of 12, 16 and 24 impact and penetrate unconfined borosilicate cylinders and those under pressure-free polycarbonate, aluminum and steel confinements. The cylinders are all of the same size with projectile–target diameter ratios lying between 12 and 24, and projectile–target length ratio equal to 8. A stress wave controlling confinement is introduced to approximate an elastic waveguide set-up. Penetration depths into the comminuted borosilicate and the corresponding fragment jet diameters are measured between 168 and 1038 m/s impact velocities with high-speed photography and a witness plate. Expectedly, target resistive pressure increases with confinement impedance but decreases with projectile diameter. However, cylinders confined by steel are less resistive to penetration than those confined by aluminum. This anomalous behavior suggests that comminution increases with dynamic compression and it may be related to densification and the failure wave which occur in silica glasses above certain critical pressures. On this basis, comminution threshold conditions are determined and found to depend strongly on the propagation of stress waves across the target–confinement interface. These results are useful for material selection of impact/penetration-resistant structures with ceramic cores.

Keywords: Projectile penetration; Pressure-free confinement; Comminution; Fragment flow; Target strength; Failure wave; Densification; Ceramics; Wave impedance

* Fax: +1-617-253-8125.
E-mail address: doyoyo@mit.edu (M. Doyoyo).

0020-7683/$ - see front matter © 2003 Elsevier Ltd. All rights reserved.
doi:10.1016/S0020-7683(03)00280-4

1. Introduction

Comminution and fragment-flow are inhibited during projectile penetration of confined and pre-compressed ceramics (Shockey et al., 1990; Anderson and Morris, 1992; Sherman, 1997; Sherman and Ben-Shushan, 1998; Westerling et al., 2001). Particularly, confined fragments undergo Mohr–Coulomb flow (Klopp and Shockey, 1991; Curran et al., 1993; Sundaram, 1998) thereby consuming more projectile energy than they would in free-flow. These properties are useful for designing light-weight, impact and penetration-resistant structures with ceramic cores (Laible, 1980). In what follows, we introduce two definitions of ceramic confinement:

- *pressure confinement*: a ceramic is confined by the same material by varying the amount of confinement pressure or pre-compression,
- *impedance confinement*: a ceramic is under pressure-free confinement by different materials with different wave impedances.

Since pressure confinement is well-understood, we are presently interested in how a brittle target under an impedance confinement responds to projectile penetration. Specifically, we consider long-rod projectile penetration into borosilicate cylinders confined by polycarbonate, aluminum and steel tubes. Our experimental objectives are:

- projectiles have to remain rigid during penetration,
- borosilicate targets have to be comminuted,
- borosilicate targets are not to be perforated by the projectiles,
- it should be possible to monitor penetration and fragment-flow during testing.

The first requirement allows one to neglect the role of projectile erosion that is typical during penetration of confined ceramics. The second requirement is ideal for borosilicate because its fracture toughness is low as compared to that of ceramics. The third requirement is met by choosing borosilicate to have a diameter 12 times that of the thickest projectile, and a length eight times the fixed length of the projectiles. The fourth objective is achieved by using projectiles whose length-over-diameter (L/D) ratios range between 12 and 24.

Subject to the above objectives, we perform tests for a range of impact velocities from 168 to 1038 m/s and measure the ejecta diameter and the corresponding penetration depth into the comminuted borosilicate. We then define and determine conditions for comminution in borosilicate and evaluate resistive pressures for each confinement condition. Finally, we discuss the anomalous observation for aluminum-confined borosilicate and qualitatively explain the absence of projectile erosion in the experiments.

2. Experimental procedure

The schematic of Fig. 1 shows a high-pressure gas gun propelling a sabot carrying a long-rod projectile to impact and penetrate a confined borosilicate target. The projectile intersects two laser beams along its path. The beams are used to measure the impact velocity and to trigger the high-speed camera which together with the witness plate monitors penetration and fragment-flow. Based on the set-up in Fig. 1, the depth of penetration into comminuted borosilicate and the corresponding fragment jet diameter are measured.

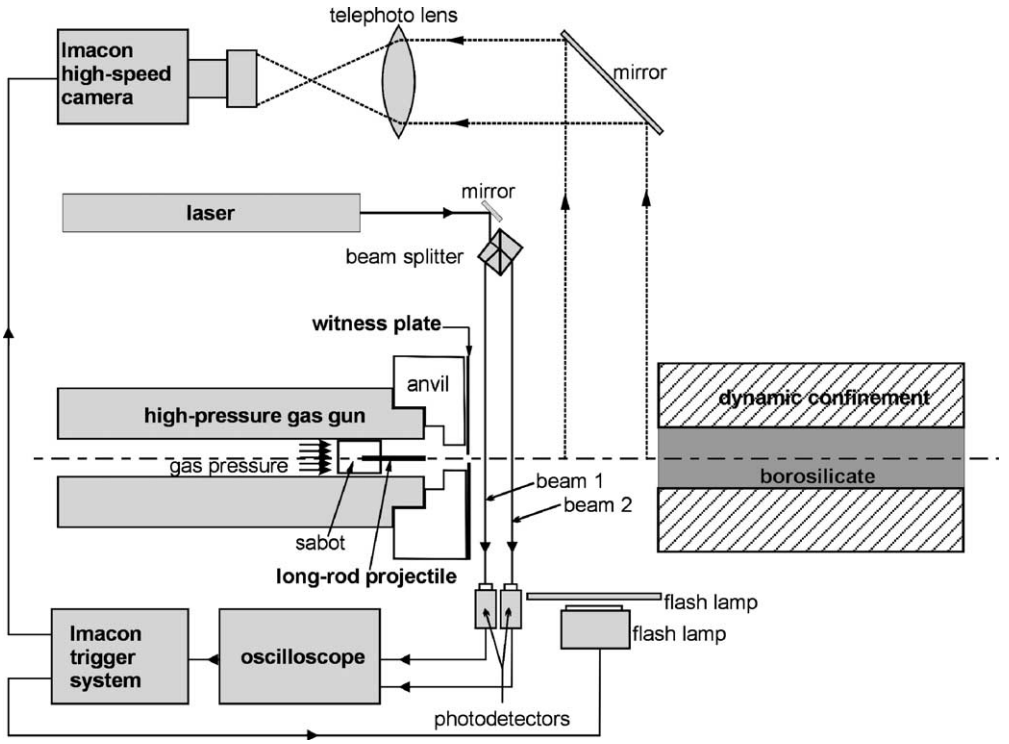

Fig. 1. A schematic of the experimental set-up used to investigate long-rod projectile penetration into borosilicate targets under impedance confinement. A high-pressure gas gun launches the rod projectile, while the penetration and fragment-flow event is monitored with a high-speed camera and a witness plate.

2.1. Material and specimen characterization

2.1.1. Projectile characteristics

High-speed tool steel (T11302-M2) rods manufactured by Allegheny Ludlum, Pittsburgh, PA, with the following alloy composition: 5.65% W, 4.65% Mo, 4.15% Cr, 1.80% V and 0.82% C are used as projectiles. Tool steel is chosen for its high fracture toughness and hardness. This enables it to resist projectile erosion over a wide impact velocity range. Table 1 lists some of its properties. It has a nominal density of $\rho_p \sim 8.14 \times 10^3$ kg/m^3. Its fracture toughness K_{IC}^p lies between 100 and 154 MPa m$^{1/2}$. It has a quasi-static compressive strength of $\sigma_p \sim 3.2$ GPa, and it is heat-treated to a Rockwell hardness of 62–64 (C Scale). Projectiles are $L_p^* = 38$ mm long (star denotes fixed length). Three different diameters are used: $D_p = 1.6$, 2.4, 3.2 mm with ratios $L_p^*/D_p = 24$, 16 and 12, respectively.

2.1.2. Target characteristics

Borosilicate glass manufactured by Schott Glaswerke, Mainz, Germany, with the following chemical composition: 80% SiO_2, 13% B_2O_3, 4% Na_2O, 2% Al_2O_3, 0.5% K_2O is used as the target. Its elastic constants are also listed in Table 1. It has a nominal density of $\rho_t \sim 2.23 \times 10^3$ kg/m^3, with longitudinal Z_t^l and shear Z_t^s wave impedances of 13.6 and 8.3×10^3 kg s/m^2, respectively. Its fracture toughness of $K_{IC}^t \sim$ 0.8 MPa m$^{1/2}$ is less than a quarter that of alumina (3–6 MPa m$^{1/2}$), while its compressive strength σ_t is only

Table 1
Mechanical properties of tool steel projectile and borosilicate target

	Tool-steel projectile	Borosilicate target
Density (g/cm^3)	8.1	2.2
Young's modulus (GPa)	204	74
Elastic Poisson's ratio	0.3	0.2
Longitudinal wave speed (km/s)	5.8	6.1
Shear wave speed (km/s)	3.1	3.7
Longitudinal wave impedance (10^6 kg s/m^2)	47.2	13.6
Shear wave impedance (10^6 kg s/m^2)	25.2	8.3
Fracture toughness (MPa m$^{1/2}$)	100–154	0.8
Compressive strength (GPa)	3.2	1.2
Rockwell hardness (C Scale)	62–64	48

1.2 GPa. The cylinders are $L_t^* = 305$ mm long with a diameter of $D_t^* = 38$ mm. These dimensions are large enough to avoid target perforation.

2.1.3. Confinement characteristics

Table 2 shows that the confinements are made up of materials with distinctly different wave impedances:

- mild steel (AISI 1020): with impedances about three times those of borosilicate,
- aluminum alloy (6061-T651): with impedances matching those of borosilicate,
- polycarbonate (LEXAN): with impedances about one-fifth those of borosilicate.

The schematic of the confinement is shown in Fig. 2. It consists of two half-sections with surface corrugations that act as obstacles to the transmitted stress waves at the confinement surface to prevent them from reloading the target (Kolsky, 1963). Although this design is unique for penetration, the concept has been used before for plate impact tests (Raiser et al., 1994). The present shape is favored because it is convenient for the design of specimen holders.

The confinement covers a cross-sectional area of 76 mm × 76 mm. The combination of a long target and a large confinement with surface corrugations makes the target "unbounded" in terms of stress waves. This allows stress waves to undergo successive transmission and reflection at the target–confinement interface, a behavior typical of an elastic waveguide (Graff, 1993). Finally, a thin layer of vacuum grease is applied on the surface of the cylinders to ensure a pressure-free confinement. Fig. 3 shows a photograph of borosilicate target, confinements, projectiles and sabots.

Table 2
Elastic wave properties of confinement materials

Confinement material	Density (g/cm^3)	Longitudinal wave speed (km/s)	Shear wave speed (km/s)	Longitudinal wave impedance (10^6 kg s/m^2)	Shear wave impedance (10^6 kg s/m^2)
Steel AISI 1020	7.8	5.9	3.2	46.0	25.0
Aluminum 6061-T651	2.7	6.2	3.1	16.7	8.4
Polycarbonate LEXAN	1.2	2.1	0.9	2.5	1.1
Borosilicate	2.2	6.1	3.7	13.6	8.3

The properties of borosilicate are also presented as a reference.

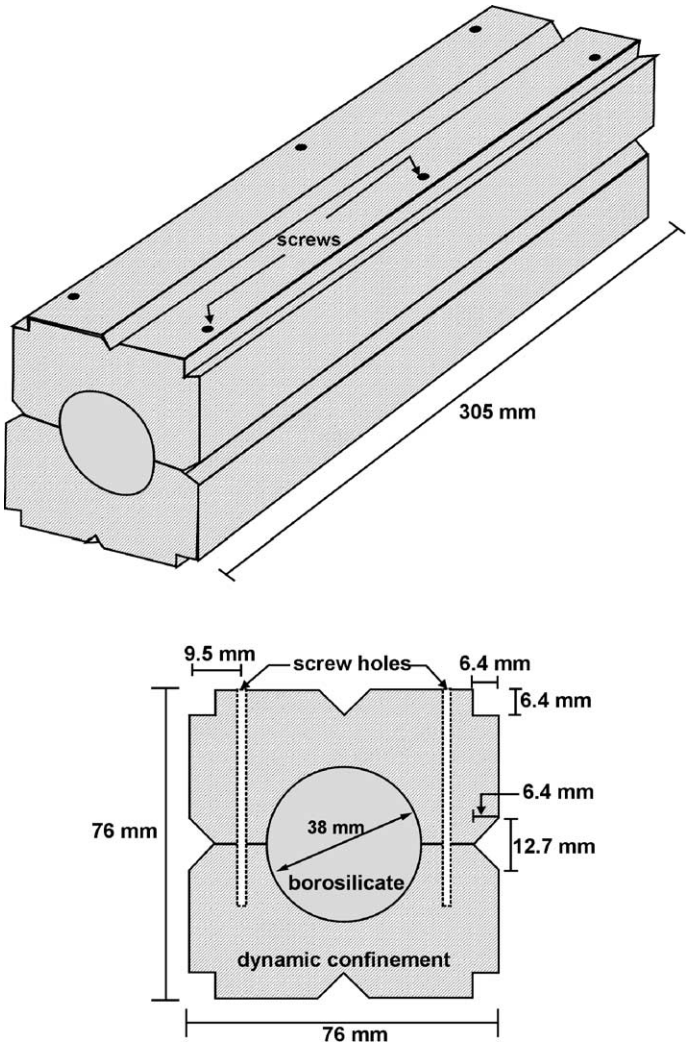

Fig. 2. A schematic of a confined borosilicate cylinder. The confinement has corrugations that act as obstacles to the incident stress waves at the confinement surface thereby preventing them from traveling back to reload the target. This set-up approximates an elastic waveguide in axi-symmetric configuration.

2.2. Measurement of experimental variables

2.2.1. Measurement of projectile impact velocity

The high-pressure gas gun shown in the schematic of Fig. 1 has a bore of diameter 12.7 mm. It launches long-rod projectiles via 19 mm long polycarbonate sabots. The sabots strike a steel anvil with a hole small enough to stop the sabots but to allow the rods to go through (Field et al., 1994). The projectiles then intersect two laser beams of 514 nm wavelengths (beam 1 and beam 2 in Fig. 1). The laser beams are provided by an argon ion laser (Coherent, Innova 300, Innova Electronics Inc., Houston, TX) and are collected by two photodetectors (350 MHz, Model DET 200, Thorlabs, Inc., North Newton, NJ). The impact velocity V_p is calculated by dividing the distance between the two laser beams by the time elapsed during the interception of the two beams. This time duration is

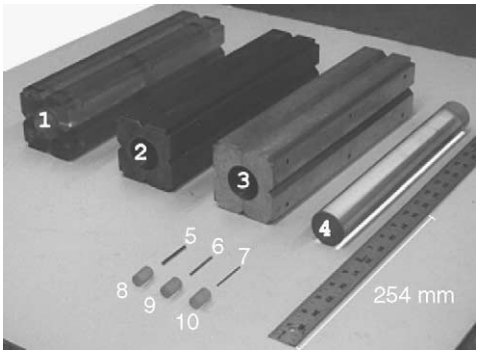

Fig. 3. A photograph of polycarbonate (1), steel (2), and aluminum (3) confinements; borosilicate target (4); the 3.2 mm diameter (5), 2.4 mm diameter (6), and 1.6 mm diameter (7) projectiles; and polycarbonate sabots (8–10).

recorded at a digital oscilloscope (1 GHz, LeCroy, Model 9374, LeCroy Corporation, Chestnut Ridge, NY).

2.2.2. Measurement of penetration depth into comminuted borosilicate

The long-rods are recovered intact after penetrating the borosilicate cylinders at impact velocities below 1038 m/s. Penetration depth is measured as the distance the projectile travels into the comminuted borosilicate. Thus, this measurement should not be confused with the depth of penetration (DOP), which is measured on the metallic backing plate after ceramic perforation (see Zukas, 1990). To emphasize this difference, we denote the current measurement of penetration depth by P_p instead of DOP.

Shallow penetration measurement: Shallow penetration is when the projectile does not remain trapped inside the comminuted borosilicate target after penetration. Recall that the length of the projectile is denoted by L_p^*. If the distance traveled by the projectile into the target relative to the impact plane is L_v, then $P_p = L_p^* - L_v$. The rods typically leave visible indentations on a lowly comminuted borosilicate, from which the length L_v is measured. High-speed photographs are also used to measure this distance.

Deep penetration measurement: Deep penetration is when the rod remains trapped inside an intensely comminuted target. If the distance between the impact plane and the final position of the submerged tail of the projectile is L_s, then $P_p = L_p^* + L_s$. The distance L_s is measured directly after penetration.

2.2.3. Measurement of fragment jet diameter

The fragment jet which is formed when the projectile is penetrating the target is monitored with a high-speed camera (Imacon 790, Hadland Photonics, Tring, UK). An inter-frame time of 40 μs is used. The lighting for the high-speed photographs is provided by two flash lamps (Model U-2MF, Hadland Photonics, Tring, UK) with a diffuser placed in front of them for uniform lighting. The high-speed camera and the flash lamps are controlled by a pulse delay generator (Stanford Research Systems, Inc., 1 GHz, 50 Ω Model DG 535, Stanford, CA), which is triggered when laser beam 2 in Fig. 1 is intersected by the rod. The generator is set to appropriate delay times between 60 and 700 μs depending on the expected impact velocity. Two different methods are used to measure the fragment jet.

High-speed photography measurement: Fig. 4 shows a fragment jet in a sequence of high-speed photographs during penetration of an *unconfined borosilicate* cylinder by a 2.4 mm diameter rod which had impacted the cylinders at 236 m/s. The photographs show that the fragment jet diameter increases to a constant value after some elapsed time (frames 6 to 7). The same observation is shown quantitatively with high-speed photographs in Figs. 5 and 6 ($V_p = 360$ m/s and $D_p = 2.4$ mm, and $V_p = 250$ m/s and $D_p = 3.2$ mm for Figs. 5 and 6, respectively) for penetration into unconfined borosilicate. Note that for fragments

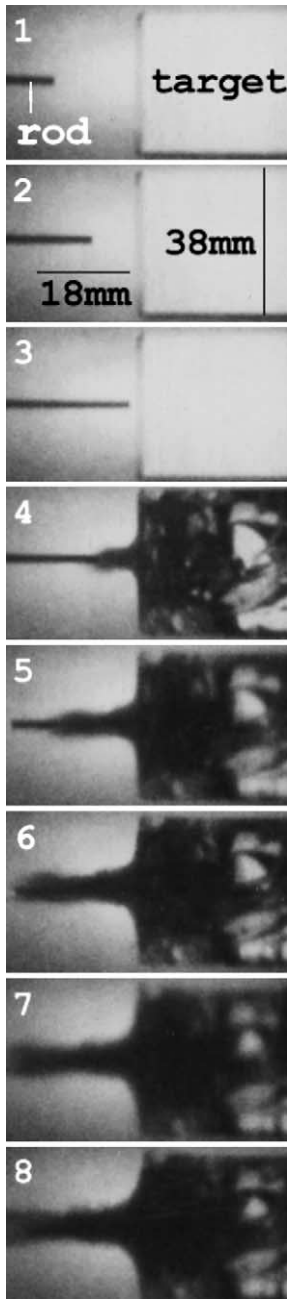

Fig. 4. A sequence of high-speed photographs showing the behavior of the fragment jet during penetration of *unconfined borosilicate* impacted at 236 m/s by a projectile of 2.4 mm diameter. The time between photographic frames is 40 μs.

ejected at a higher impact velocity, the fragment jet diameter at the "throat" still becomes saturated (Fig. 5). Based on these observations, we define the *saturated* or *final* fragment jet as the diameter at the throat of the jet D_j. In Figs. 5 and 6, $D_j/D_p = 10.8\ \text{mm}/2.4\ \text{mm} = 4.5$ and $D_j/D_p = 14.3\ \text{mm}/3.2\ \text{mm} = 4.5$,

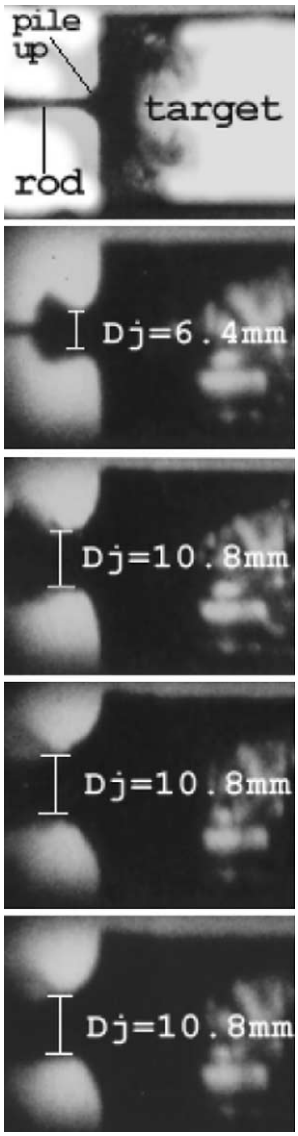

Fig. 5. A sequence of high-speed photographs showing the saturation of the fragment jet diameter during penetration of an *unconfined borosilicate* impacted at 360 m/s by a projectile of 2.4 mm diameter. The time between photographic frames is 40 μs. Note that $D_j/D_p = 10.8$ mm/2.4 mm ~ 4.5 for this example.

respectively. Thus D_j/D_p is the same for the two cases. Note that the thicker projectile has the same D_j/D_p as the thinner projectile, although the impact velocities are different. Thus, D_j/D_p depends on the impact velocity.

Witness plate measurement: The witness plate is made up of a 1 mm lead sheet covered by a double-sticker tape rigidly placed between the anvil and the target. The use of a witness plate to investigate fragment flow is not new (Kipp and Grady, 1995). Fig. 7 shows the fragment jet diameter measurement on a witness plate for penetration into *polycarbonate-confined borosilicate*. The loading condition for the example in Fig. 7 is: $V_p = 280$ m/s and $D_p = 3.2$ mm. Based on this example, $D_j/D_p = 6.5$ mm/3.2 mm $= 2$.

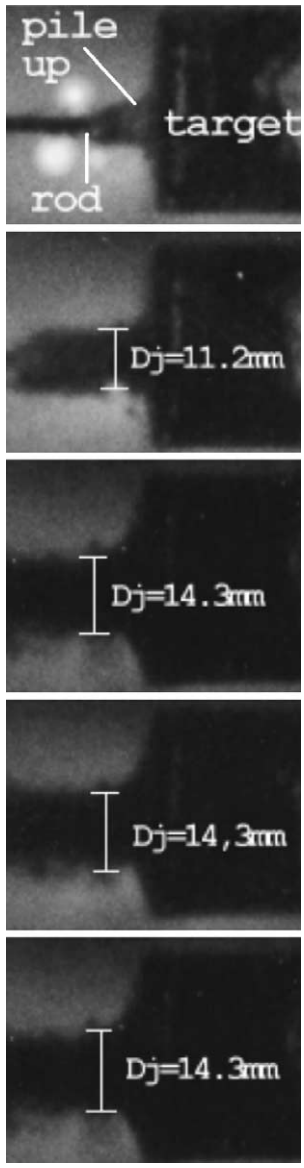

Fig. 6. A sequence of high-speed photographs showing the saturation of the fragment jet diameter during penetration of an *unconfined borosilicate* impacted at 250 m/s by a projectile of 3.2 mm diameter. The time between photographic frames is 40 μs. Note that $D_j/D_p = 14.3$ mm/3.2 mm ~ 4.5 for this example.

Recall that $D_j/D_p = 4.5$ for the unconfined borosilicate when $V_p = 250$ m/s. Therefore, D_j/D_p is also sensitive to confinement condition.

2.2.4. Final remarks on the measurement of experimental variables

Note that the fragment jet diameter is not equal to the crater diameter as it depends on fragment flow, while the crater diameter depends on the degree of comminution. It is possible that some fragments on the

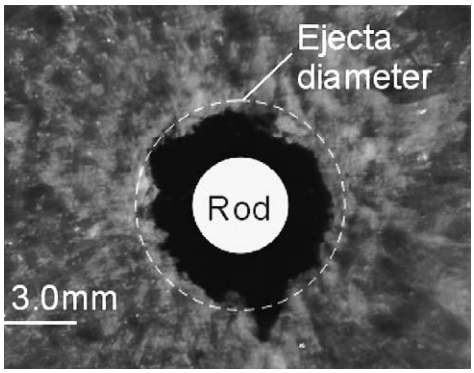

Fig. 7. A photograph of a recovered witness plate showing how it was used to measure the fragment jet diameter. This particular example shows the resulting measurement of the ejecta diameter for *polycarbonate-confined borosilicate* impacted at 280 m/s by a projectile of diameter 3.2 mm. Note that $D_j/D_p = 6.5$ mm/3.2 mm ~ 2 for this example.

comminuted target may remain stagnant during projectile penetration, so that the crater diameter is generally larger than the fragment jet diameter. The more the impact velocity is increased, the more it becomes increasingly difficult to measure the correct final penetration depth into unconfined comminuted borosilicate. Thus, several layers of a bubble wrap (3/16 inch diameter bubbles) are wrapped around the cylinders. Tight O-rings are fitted around the wrap before fitting the whole assembly into a metal tube of appropriate size. This does not affect the measurements as the bubble wrap has negligible impedances and acts as a free-surface.

3. Results and discussions

A series of tests are conducted on unconfined and confined borosilicate between 168 and 1038 m/s impact velocities. The minimum velocity of 168 m/s denotes that comminution has occurred in unconfined borosilicate. In this study, projectile erosion is not acceptable (see Section 1). Note that the maximum velocity before erosion occurs depends on projectile size and confinement condition (see Table 3): so that, it is 1038 m/s for 1.6 mm diameter projectile. The measured quantities are: final penetration depth (P_p) and final fragment jet diameter (D_j). The controlled quantities are: impact velocity (V_p), dynamic confinement condition (K) and projectile diameter (D_p). The fixed quantities are: projectile length (L_p^*), borosilicate length (L_t^*) and borosilicate diameter (D_t^*).

3.1. Raw data

Table 3 lists the average values of the measured quantities ($\widehat{P}_p, \widehat{D}_j$). The tests involving unconfined and polycarbonate-confined borosilicate are repeated for a maximum of three times per loading condition. However, tests involving aluminum-confined and steel-confined borosilicate are repeated more than three times because of the counter-intuitive observation to be reported later. This is not by any means the best statistical representation of the data, yet the standard deviations are always within 10% of the average quantities. Penetration depth $\widehat{P}_p$ and fragment jet diameter $\widehat{D}_j$ as functions of projectile impact velocity V_p are plotted in Figs. 8–10 and Figs. 11–13, respectively for each projectile diameter D_p. Important observations which can be deduced are:

Table 3
Average penetration depth and the corresponding average fragment jet diameters for projectile penetration into confined borosilicate targets

D_p (mm)	V_p (m/s)	Unconfined borosilicate		Polycarbonate-confined borosilicate		Aluminum-confined borosilicate		Steel-confined borosilicate	
		$\widehat{P}_p$ (mm)	$\widehat{D}_j$ (mm)	$\widehat{P}_p$ (mm)	$\widehat{D}_j$ (mm)	$\widehat{P}_p$ (mm)	$\widehat{D}_j$ (mm)	$\widehat{P}_p$ (mm)	$\widehat{D}_j$ (mm)
3.2	168	–	3.4	–	–	–	–	–	–
3.2	265	8.0	7.6	5.0	5.5	–	4.2	6.7	5.2
3.2	335	12.5	8.0	–	–	–	–	–	–
3.2	375	16.0	10.0	11.4	8.0	8.0	6.0	10.3	7.4
3.2	410	19.0	11.5	–	–	–	–	–	–
3.2	459	26.5	12.4	16.7	9.6	9.9	9.0	14.1	9.8
3.2	503	29.0	13.0	–	–	–	–	–	–
3.2	530	32.8	13.8	20.5	12.8	12.4	11.2	17.9	12.2
3.2	556	35.0	15.0	–	–	–	–	–	–
3.2	592	38.0	17.0	26.6	–	13.7	11.5	22.0	14.7
3.2	620	–	–	28.9	15.8	–	–	25.1	15.2
3.2	649	41.0	18.5	30.8	17.0	16.3	14.1	–	–
3.2	701	49.0	19.5	–	–	17.1	14.1	–	–
3.2	749	–	–	–	–	22.4	16.6	–	–
3.2	795	–	–	–	–	21.3	18.1	–	–
3.2	838	–	–	–	–	26.4	19.2	–	–
2.4	188	–	3.0	–	–	–	–	–	–
2.4	298	7.5	7.5	7.6	–	–	4.5	6.1	5.5
2.4	377	11.5	10.5	–	–	–	–	–	–
2.4	421	16.0	11.0	10.6	10.2	8.4	6.6	9.1	9.3
2.4	461	19.0	11.4	–	–	–	–	–	–
2.4	516	22.0	12.8	14.8	11.6	9.9	8.6	12.2	10.5
2.4	565	26.0	13.0	–	–	–	–	–	–
2.4	595	26.5	13.5	19.0	13.9	11.8	10.1	15.2	13.0
2.4	625	27.0	14.0	–	–	–	–	–	–
2.4	666	31.5	16.0	25.1	15.0	15.6	12.0	18.1	14.5
2.4	729	36.0	17.1	–	–	14.1	13.2	–	–
2.4	788	39.5	18.3	–	–	17.9	15.1	–	–
2.4	842	–	–	–	–	19.4	16.1	–	–
2.4	893	–	–	–	–	22.4	17.2	–	–
2.4	941	–	–	–	–	23.9	18.1	–	–
1.6	328	9.0	4.5	–	–	–	–	–	–
1.6	382	–	–	5.7	–	–	4.0	6.8	–
1.6	464	15.0	7.0	10.3	7.2	8.0	5.4	8.0	6.7
1.6	508	16.5	–	–	–	–	–	–	–
1.6	569	–	–	14.1	8.3	9.1	7.0	11.0	7.8
1.6	600	20.0	8.4	–	–	–	–	–	–
1.6	656	23.5	9.6	17.5	9.6	11.8	8.6	13.4	9.1
1.6	734	27.5	11.0	20.9	11.2	13.7	9.6	16.0	10.4
1.6	804	32.0	12.2	25.1	–	14.4	10.6	17.9	11.8
1.6	868	35.0	12.8	25.5	–	17.5	12.6	–	–
1.6	928	–	–	–	–	17.9	12.6	–	–
1.6	985	–	–	–	–	19.8	13.6	–	–
1.6	1038	–	–	–	–	23.2	15.0	–	–

- penetration depth and fragment jet diameter are highest for unconfined borosilicate and lowest for aluminum-confined borosilicate,
- penetration depth and fragment jet diameter increase with projectile diameter,
- penetration depth is higher for steel-confined borosilicate than for aluminum-confined borosilicate.

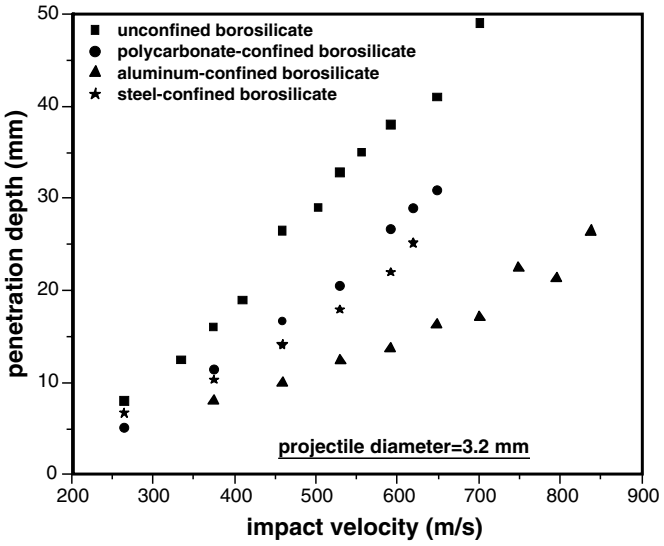

Fig. 8. The role of impedance confinement on the penetration depth into comminuted borosilicate impacted and penetrated by projectiles of diameter 3.2 mm.

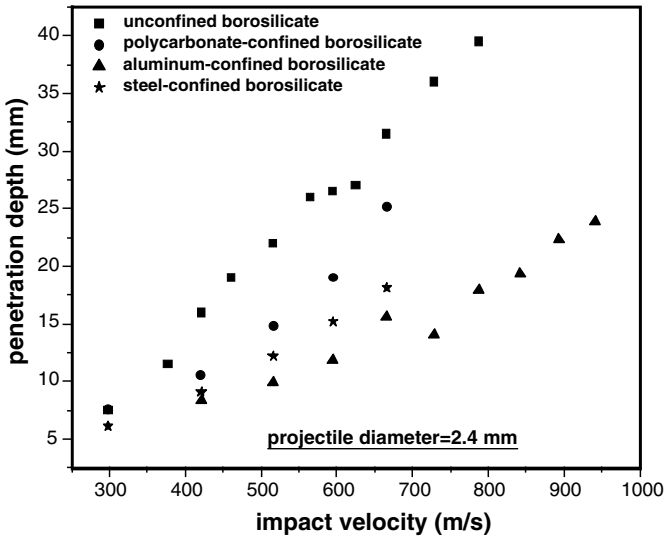

Fig. 9. The role of impedance confinement on the penetration depth into comminuted borosilicate impacted and penetrated by projectiles of diameter 2.4 mm.

3.2. Dimensional and least-squares analysis

The relations among the measured quantities $(\widehat{P}_{\mathrm{p}}, \widehat{D}_{\mathrm{j}})$ and the experimental variables $(V_{\mathrm{p}}, D_{\mathrm{p}}, K)$ are now established using dimensional and least-squares analysis. We first introduce a dimensionless number (η), which is the ratio of the original projectile kinetic energy density to the *quasi-static* cavity-expansion pressure R_{t}. For a projectile of density ρ_{p} striking the borosilicate target at velocity V_{p}, we have

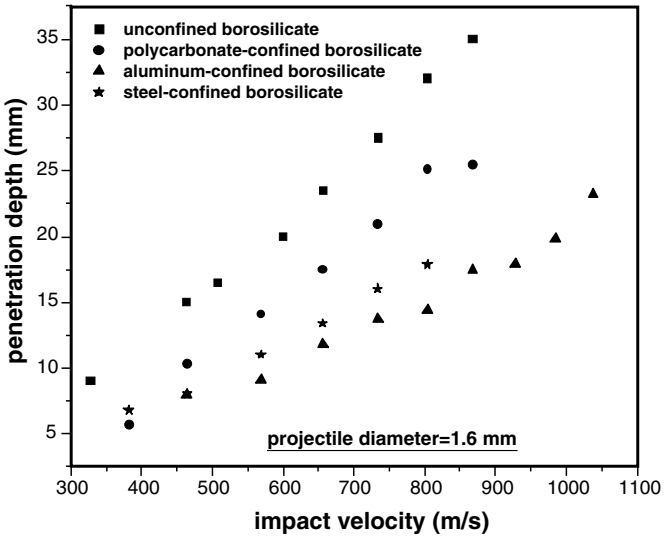

Fig. 10. The role of impedance confinement on the penetration depth into comminuted borosilicate impacted and penetrated by projectiles of diameter 1.6 mm.

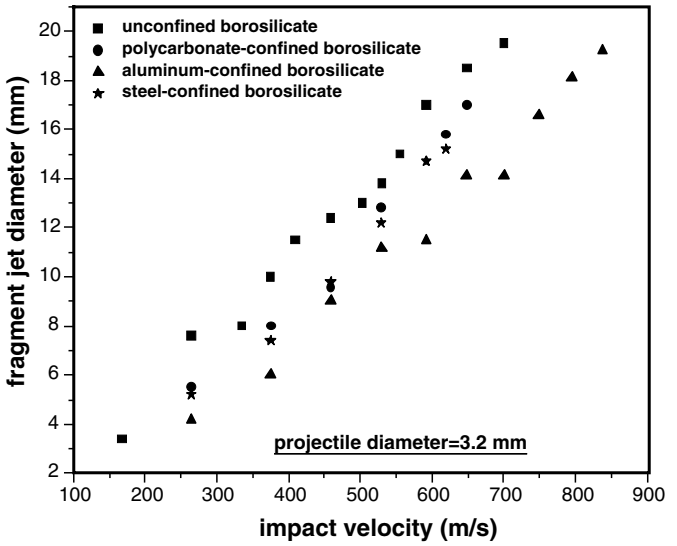

Fig. 11. The role of impedance confinement on the fragment jet diameter for borosilicate impacted and penetrated by projectiles of diameter 3.2 mm.

$$\eta = \frac{\rho_p V_p^2/2}{R_t} = \frac{V_p^2}{V_0^2} \tag{1}$$

where $V_0 = \sqrt{2R_t/\rho_p}$. This quantity, although it has units of L/T is not a measure of velocity! It is also not defined for situations where projectile erosion occurs because the cross-section of the projectile–target interface varies with penetration. Note that R_t should be distinguished from the *dynamic* cavity expansion

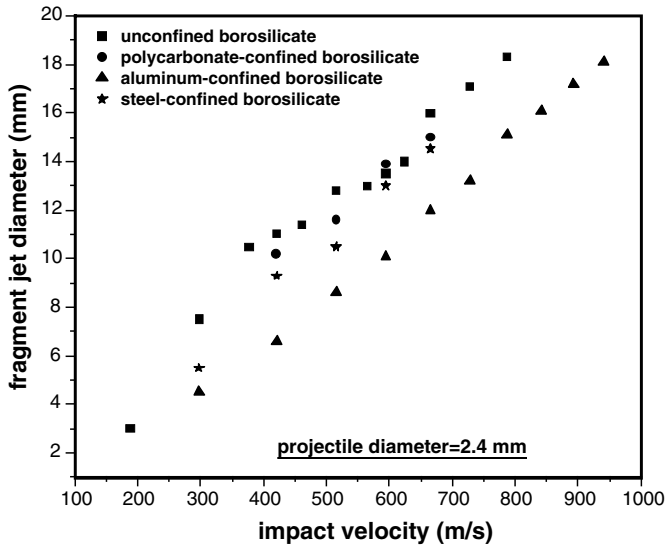

Fig. 12. The role of impedance confinement on the fragment jet diameter for borosilicate impacted and penetrated by projectiles of diameter 2.4 mm.

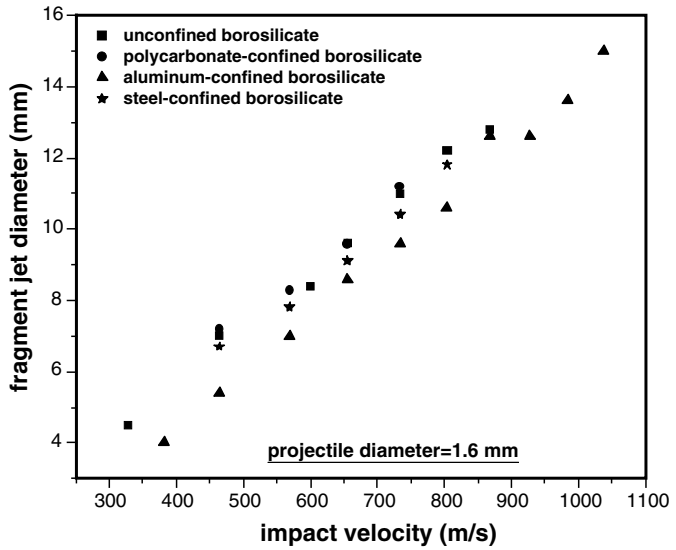

Fig. 13. The role of impedance confinement on the fragment jet diameter for borosilicate impacted and penetrated by projectiles of diameter 1.6 mm.

pressure which is a function of projectile velocity (Forrestal and Longcope, 1990; Satapathy and Bless, 1996). For quasi-static penetration into a compressible, elastic plastic, non-hardening material, R_t is given by Bishop et al. (1945) as

$$R_t = \frac{2}{3}\sigma_t\left[1 + \ln\frac{E}{3\sigma_t(1-\nu_t)}\right] \tag{2}$$

where σ_t is the compressive strength, E_t is the Young's modulus and ν_t is the plastic Poisson's ratio of the target. For borosilicate, these quantities are listed in Table 1: $\sigma_t \sim 1.2$ GPa, $E_t \sim 74$ GPa and $\nu_t \sim 0.2$. Using these values, we get $R_t \sim 3.4$ GPa for borosilicate. The density of tool steel in Table 1 is $\rho_p \sim 8.14 \times 10^3$ kg/m^3 so that $V_0 \sim 914$ m/s. Based on the measurements, $\widehat{P}_p$ and $\widehat{D}_j$ depend on impact velocity, projectile diameter and confinement. Then, in dimensionless form, we have

$$\widetilde{P}_p = \varphi_1(\sqrt{\eta}, K) \tag{3}$$

$$\widetilde{D}_j = \varphi_2(\sqrt{\eta}, K) \tag{4}$$

where $\widetilde{P}_p = \widehat{P}_p/D_p$, $\widetilde{D}_j = \widehat{D}_j/D_p$. After least-squares analysis of the data in Table 3 with respect to $\sqrt{\eta}$, we find

$$\widetilde{P}_p \approx \xi_0(K) + \xi_1(K)\eta \tag{5}$$

$$\widetilde{D}_j \approx \alpha_0(K) + \alpha_1(K)\sqrt{\eta} \tag{6}$$

The values of $\xi_0(K)$, $\xi_1(K)$, $\alpha_0(K)$ and $\alpha_1(K)$ are listed in Table 4, while the variations of $\widetilde{P}_p$ and $\widetilde{D}_j$ with $\sqrt{\eta}$ are shown in Figs. 14 and 15, respectively.

3.3. Physical interpretation

In the present axi-symmetric test configuration; the stress waves propagate in the long borosilicate cylinders the same way that they would in an elastic waveguide. This means that, mechanical waves undergo successive reflection and transmission at the target–confinement interface as they travel through the cylinder. Thus, the reflected waves alternate between tensile-shear and compressive-shear states inside the target, while their amplitudes continue to decrease with time. The exact contributions of mechanical wave impedances require a full-scale numerical simulation of the penetration event which is not the focus of the present study. From simple considerations of the propagation of a longitudinal wave across a planar target–confinement interface (Meyers, 1994) as well as that comminution in glass is a well-controlled cooperative dynamic fracture process, one would expect steel-confined targets to be stronger than aluminum-confined targets. However, our experimental results are contrary to this argument as aluminum-confined targets turn out to be stronger than steel-confined targets. Although the use of conventional failure kinetics of dynamic fracture is an easily-acceptable approach for low pressures, its main weakness for high pressures is that it excludes the role of instability phenomena that are typical in silica glasses above certain critical pressures.

Therefore, we introduce the concept of threshold conditions of comminution to compare the response of borosilicate under different impedance confinement. We are assuming that comminution is an instability directly related to densification and the generation of a failure wave in borosilicate. These two phenomena are commonly observed in silica glasses above certain threshold pressures (for failure waves: see

Table 4
Confinement-dependent parameters of penetration and fragment flow as determined from least-squares analysis for confined borosilicate

	$\xi_0(K)$	$\xi_1(K)$	$\alpha_0(K)$	$\alpha_1(K)$
Unconfined borosilicate	1.77	22.66	−0.25	8.87
Polycarbonate-confined borosilicate	0.41	19.31	−1.08	9.78
Aluminum-confined borosilicate	1.10	9.32	−1.55	9.01
Steel-confined borosilicate	1.24	13.16	−1.07	9.39

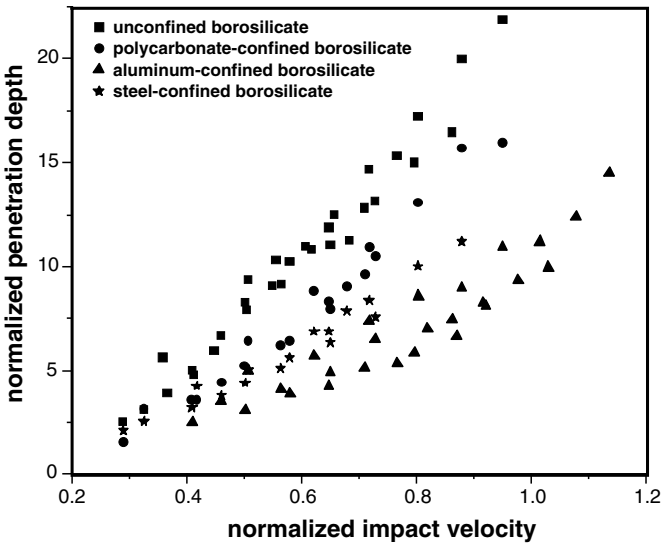

Fig. 14. The role of impedance confinement on penetration depth into comminuted borosilicate. The impact velocity is normalized by V_0, while the penetration depth is normalized by D_p.

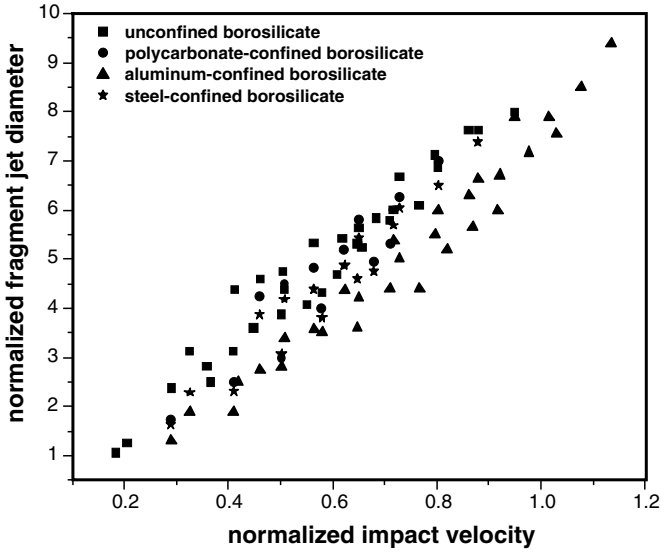

Fig. 15. The role of impedance confinement on fragment jet diameter into comminuted borosilicate. The impact velocity is normalized by V_0, while the fragment jet diameter is normalized by D_p.

Kanel et al., 1991; Brar et al., 1991; Clifton, 1993; Bourne et al., 1998, for densification: see Bridgman and Simon, 1953; Sugiura and Yamadaya, 1992). But, we have no experimental evidence supporting this claim or any other such evidence by other investigators; although the failure wave connection to ceramic penetration has been made (see Zilberbrand et al., 1999; Satapathy et al., 1999).

3.3.1. Threshold conditions of comminution

We assume that there exists an impact velocity V_p^* above which borosilicate is comminuted and the projectile will subsequently penetrate the target, thus creating a fragment jet. In other words, D_j is always greater than D_p when fragments are being ejected from the comminuted target. We will refer to this velocity as the *threshold velocity of comminution*, which is obtained from Eq. (6) by letting $\widetilde{D}_j \geqslant 1$, that is

$$V_p^* \geqslant V_0 \left[\frac{1 - \alpha_0(K)}{\alpha_1(K)} \right] \tag{7}$$

The dynamic compressive stress in the target associated with V_p^* is referred to as the *threshold stress of comminution* σ_t, which is given by

$$\sigma_t^* \geqslant \rho_t c_t V_p^* = \rho_t c_t V_0 \left[\frac{1 - \alpha_0(K)}{\alpha_1(K)} \right] \tag{8}$$

Borosilicate has $\rho_t \sim 2.23 \times 10^3$ kg/m^3 and $c_t \sim 6.1$ km/s, while $\alpha_0(K)$ and $\alpha_1(K)$ are listed in Table 4. The values of V_p^* and σ_t are calculated from the above two equations and then listed in Table 5. The threshold velocity of 128 m/s is required to comminute unconfined borosilicate, while the threshold velocity of 259 m/s is required to comminute aluminum-confined borosilicate. The failure wave in silica glass is observed at a dynamic compressive stress of $\sigma_t^f \sim 2.4$ GPa (Brar et al., 1991). Therefore, we also list σ_t^*/σ_t^f in Table 5. The threshold stresses of comminution for different confinement situations are close to the failure wave stress. However, the threshold stress of aluminum-confined borosilicate is exceptionally 1.5 times the failure wave stress.

3.3.2. Average target resistive pressure

We define the average target resistive pressure $\widehat{R}$ as the original energy available for penetration per unit volume penetrated. Following the results of the previous section, we assume that the projectile will continue to penetrate the target as long as its velocity drops below V_p^*. This means that

$$\widehat{R} = \frac{1}{\Omega_p} (\rho_p A_p L_p^* V_p^2 - \rho_p A_p L_p^* V_p^{*2}) \tag{9}$$

where $\Omega_p = P_p A_p$ is the volume penetrated, A_p is the cross-sectional area of the projectile. Note that this definition of $\widehat{R}$ implies that the projectile remains rigid during penetration, which is also consistent with our experiments. Normalizing $\widehat{R}$ by R_t, we get

$$\frac{\widehat{R}}{R_t} = \frac{L_p^*}{P_p} \left(\frac{V_p^2}{R_t/\rho_p} - \frac{V_p^{*2}}{R_t/\rho_p} \right) = \frac{L_p^*}{P_p} (\eta - \eta^*) \tag{10}$$

where $\eta^* = V_p^{*2}/V_0^2$. Eliminating P_p in the above equation using Eq. (5), we get

$$\frac{\widehat{R}}{R_t} = \frac{L_p^*}{D_p} \left[\frac{\eta - \eta^*}{\xi_0(K) + \xi_1(K)\eta} \right] \tag{11}$$

Table 5
Threshold conditions of comminution for confined borosilicate

	V_p^* (m/s)	σ_t^* (GPa)	σ_t^*/σ_t^f
Unconfined borosilicate	129	1.81	0.75
Polycarbonate-confined borosilicate	194	2.73	1.14
Aluminum-confined borosilicate	259	3.63	1.51
Steel-confined borosilicate	201	2.83	1.18

The threshold stresses are referenced to the failure wave stress $\sigma_t^f \approx 2.4$ GPa.

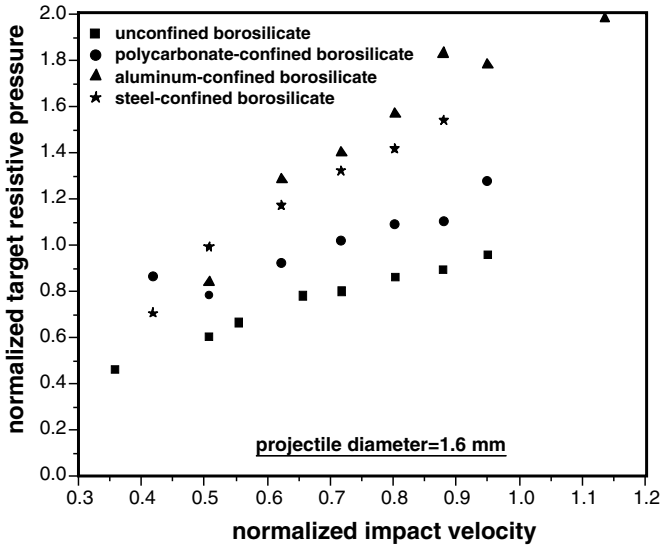

Fig. 16. The role of impedance confinement on borosilicate resistive pressure during projectile penetration. The target resistive pressure is normalized by R_t, while the impact velocity is normalized by V_0.

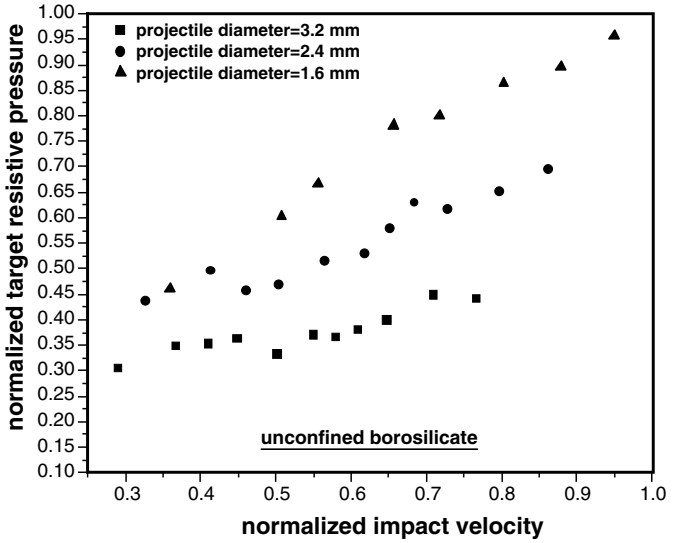

Fig. 17. The role of projectile diameter on borosilicate resistive pressure during projectile penetration. The target resistive pressure is normalized by R_t, while the impact velocity is normalized by V_0.

Thus, the average target resistive pressure is a function of impact velocity, projectile diameter and confinement. Fig. 16 gives $\widehat{R}$ as a function of $\sqrt{\eta}$ for confined borosilicate penetrated by a 1.6 mm diameter rod. Fig. 17 gives $\widehat{R}$ as a function of $\sqrt{\eta}$ for unconfined borosilicate penetrated by 1.6, 2.4 and 3.2 mm diameter rods. These two representative plots show that the resistance is highest for aluminum-confined borosilicate and lowest for unconfined-borosilicate, while it is highest for the thinnest rods and lowest for the thickest rods.

3.4. Counter-intuitive observation

Borosilicate confined by materials with increasingly higher wave impedances than it should have been harder to penetrate because of dynamic re-compression applied by the reflected stress waves. Yet, those cylinders which were confined by steel were less resistive to penetration than those confined by aluminum. Conventionally, borosilicate, like ceramics, should fracture easily when subjected to tension-shear than when under compression-shear. Thus, the observation that penetration depth is higher for steel-confined borosilicate than for aluminum-confined borosilicate is anomalous because it implies that comminution is more intense under increasing dynamic compression. In the previous section, we assumed that comminution in borosilicate is directly related to the failure wave and densification. Previous studies have shown that comminution of glasses and ceramics increase with dynamic compression on the basis of these two phenomena (Doyoyo, 2002). This theory is based on the assumption that comminution occurs behind a propagating failure wave which is caused by a type of instability involving the roughening of a densification interface. It is assumed that once densified, a region will tend to shrink, straining the interface between it and the original solid. Strained interfaces are unstable and may roughen (Freund and Jonsdottir, 1993). This event will cause tension and shear build-up behind the densification interface which will then comminute the material (Doyoyo, 2002). Although we are confident that this explanation of comminution is correct because it is related directly to the phenomena that occur in silica glasses under high pressure, we have to be cautious: Meaning that, the theory is as yet to be verified experimentally!

3.5. Absence of projectile erosion

All projectiles are recovered roughly intact below 1038 m/s. The occurrence of projectile erosion for a given range of impact velocities depends on the projectile–target material combinations. Previous micromechanical studies demonstrate the dynamics of fragment–projectile interactions which may cause erosion (Shockey et al., 1990; Kipp and Grady, 1995; Curran et al., 1993). The confined fragmented zone has also been investigated (Klopp and Shockey, 1991; Sundaram, 1998). Due to their acquired kinetic energy during penetration, the fragments may erode the projectile by a process of frictional shear flow. Let us assume that the frictional dissipation due to fragment-flow is given by $U_f = \int \tau_{eff}\, d\gamma$ (Here, γ is the shear strain and $\tau_{eff} = \tau_{M\text{–}C} + \tau_B$ is the effective shear stress). For fragments within the close vicinity of the projectile, erosion would occur provided $U_f \geqslant U_{wear}$. Here U_{wear} is the wear resistance of the projectile material. This quantity may decrease with increasing temperature T because a large amount of heat is typically generated during an impact event, thus $U_{wear} = U_{wear}(T)$. The quantity $\tau_{M\text{–}C} = \mu p$ is the shear stress due to the Mohr–Coulomb flow and p is the pressure, which depends on the confinement pressure $p_{precomp}$, confinement impedance K, and "comminution-induced" pressure $p_{induced}$, thus $p = p(p_{precomp}, K, p_{induced})$. For the present case of impedance confinement, $p_{precomp} \approx 0$ or $p = p(K, p_{induced})$. Note that the reflected waves apply alternative states of either compression-shear or tension-shear on the confined media that diminish as they propagate along a waveguide type target. This means that the contribution of impedance confinement on the pressure may be neglected, then $p \approx p_{induced}$. The comminution-induced pressure is generated by the tendency of the created comminuted media to increase its volume in a tight confinement. This is because a random assembly of granular constituents is freely-packed in a container with a volume fraction less than 1 (Bideau and Dodds, 1991). If such a media is forced to occupy a finite space, then a volumetric strain is generated. The presence of a thin layer of vacuum grease makes the present confinement not intact so that this strain may be ignored, or $p_{induced} \approx 0$. This eliminates the Mohr–Coulomb contribution to frictional flow in the present experiment altogether. The quantity $\tau_B \sim \rho_f d_f^2 \dot{\gamma}^2$ is the rate-dependent shear stress (Bagnold, 1954) for free fragment flow. Here, ρ_f is the fragment density, d_f is the fragment diameter, and $\dot{\gamma}$ is the shear strain rate. The fragments may still be reduced further due to fragment–fragment collisions so that $d_f = d_f(\gamma, \dot{\gamma})$. The fragment sizes $d_f \sim 0.01$–5 μm around the nose of the projectile for the current experiments, thus

$\tau_B \sim 0.00002 - 0.011\ \dot{\gamma}^2$ which is less than 0.2–110 MPa for $\dot{\gamma} < 10^5\ s^{-1}$. Thus, conservatively, projectile erosion can be prevented over a wide range of impact velocities in the present experimental set-up. Numerical simulation can give deeper insight on this problem as there are too many variables involved for a sufficient qualitative explanation.

4. Conclusions

Experimental results presented in this study reveal the important role played by confinement impedance on the failure kinetics of ceramics subjected to impact loading. Thin long-rods impacted and penetrated borosilicate cylinders confined by polycarbonate, aluminum and steel tubes between 168 and 1038 m/s impact velocities. High-speed photography and a witness plate were used to monitor penetration. The rod penetration depth into the comminuted borosilicate and the corresponding final fragment jet diameter were measured for a given impact velocity, projectile diameter and confinement material. The variations of the measured quantities were examined using dimensional and least-squares analysis. An explanation of the behavior of the measured quantities was given by assuming that comminution in silica glass is a dynamic instability associated with densification and the failure wave; yet the underlying mechanisms responsible for it are still not known. Based on the concept of comminution instability, threshold conditions of comminution of borosilicate and the target resistive pressures were defined and determined from the data. The threshold comminution stresses of borosilicate were found to be of the order of the critical failure wave stress but also depended on the confinement impedance. Penetration depth and fragment jet diameter increased with confinement impedance and decreased with projectile diameter. Penetration depth into steel-confined borosilicate was counter-intuitively higher than into aluminum-confined borosilicate.

Acknowledgements

The author acknowledges Professor K.-S. Kim for useful discussions. The support of the Research Fellowship from the School of Engineering at MIT and the Center for Advanced Materials Research at Brown University is greatly appreciated.

References

Anderson, C.E., Morris, B.L., 1992. The ballistic performance of confined Al203 ceramic tiles. Int. J. Imp. Eng. 12, 167–187.

Bagnold, R.A., 1954. Experiments on a gravity-free dispersion of large solid spheres in a Newtonian fluid under shear. Proc. Roy. Soc. London A 225, 49–63.

Bideau, D., Dodds, J., 1991. Granular Media: An Interdisciplinary Approach. In: Les Houche Series. Nova Science, Commack, NY.

Bishop, R.F., Hill, R., Mott, N.F., 1945. The theory of indentation and hardness test. Proc. Physical Soc. 57, 147–159.

Bourne, N., Millet, J., Murray, N., 1998. On the shock induced failure of brittle solids. J. Mech. Phys. Solids 46, 1887–1908.

Brar, N.S., Rosenberg, G.Z., Bless, S.J., 1991. Impact-induced failure waves in glass bars and plates. Appl. Phys. Lett. 59, 3396–3398.

Bridgman, P.W., Simon, I., 1953. Effects of very high pressures on glass. J. Appl. Phys. 24, 405–413.

Clifton, R.J., 1993. Analysis of failure waves in glasses. Appl. Mech. Rev. 48, 540–546.

Curran, D.R., Seaman, L., Cooper, T., Shockey, D.A., 1993. Micromechanical model for comminution and granular flow of brittle materials under high-strain rate application to ceramic targets. Int. J. Imp. Eng. 13, 53–83.

Doyoyo, M., 2002. A theory of the densification induced fragmentation in glasses and ceramics under dynamic compression. Int. J. Solids Struct. 39, 1833–1843.

Field, J.E., Walley, S.M., Bourne, N.K., Huntley, J.M., 1994. Experimental methods at high-rates of strain. J. de Physique IV 4, 3–22.

Forrestal, M.J., Longcope, D.B., 1990. Target strength of ceramic materials for high-velocity penetration. J. Appl. Phys. 67, 3669–3672.

Freund, L.B., Jonsdottir, F., 1993. Instability of a biaxially stressed thin film on a substrate due to material diffusion over its surface. J. Mech. Phys. Solids 41, 1245–1264.

Graff, K.F., 1993. Wave Motion in Elastic Solids. Ohio State University Press, Columbus, OH.

Kanel, G.I., Rosorenov, S.V., Fortov, V.E., Abesehov, M.M., 1991. The fracture of glass under high-pressure impulsive loading. High Press. Res. 6, 225–232.

Kipp, M.E., Grady, D.E., 1995. Experimental and numerical studies of high-velocity impact fragmentation. In: Davison, L., Grady, D.E., Shahinpoor, M. (Eds.), High Pressure Shock-Compression. II. Dynamic Fracture and Fragmentation. Springer-Verlag, New York, NY.

Klopp, R.W., Shockey, D.A., 1991. The strength behavior of granulated silicon carbide at high strain rates and confining pressure. J. Appl. Phys. 70, 7318–7326.

Kolsky, H., 1963. Stress Waves in Solids. Dover Publications, New York, NY.

Laible, R.C., 1980. Ballistic Materials and Penetration Mechanics. Elsevier Publishing Company, New York, NY.

Meyers, M.A., 1994. Dynamic Behavior of Materials. John Wiley and Sons, New York, NY.

Raiser, G.F., Wise, J.L., Clifton, R.J., Grady, D.E., Cox, D.E., 1994. Plate impact response of ceramics and glasses. J. Appl. Phys. 75, 3862–3869.

Satapathy, S., Bless, S., 1996. Calculation of penetration resistance of brittle materials using spherical cavity expansion analysis. Mech. Mat. 23, 323–330.

Satapathy, S., Bless, S., Ivanov, S.M., 1999. The effects of failure wave on penetration resistance of glass. In: Proc. 18th International Symposium on Ballistics, San Antonio, TX.

Sherman, D., 1997. Quasi-static and dynamic ballistic damage mechanisms in confined ceramic tiles. J. Phys. IV 21, 1021–1026.

Sherman, D., Ben-Shushan, T., 1998. Quasi-static impact damage in confined ceramic tiles. Int. J. Imp. Eng. 21, 245–265.

Shockey, D.A., Marchand, A.H., Skaggs, S.R., Cort, G.E., Burke, M.W., Parker, R., 1990. Failure phenomenology of confined ceramic targets and impacting rods. Int. J. Imp. Eng. 9, 263–275.

Sugiura, H., Yamadaya, T., 1992. Raman-scattering in silica glass in the permanent densification region. J. Non-Cryst. Solids 144, 151–158.

Sundaram, S., 1998. Pressure-Shear Response of Ceramics. PhD Thesis. Brown University, Providence, RI.

Westerling, L., Lundberg, P., Lundberg, B., 2001. Tungsten long-rod penetration into confined cylinders of boron carbide at and above ordnance velocities. Int. J. Imp. Eng. 49, 703–714.

Zukas, J., 1990. High Velocity Impact Dynamics. John Wiley and Son, New York, NY.

Zilberbrand, E.L., Vlasov, A.S., Cazamias, J.U., Bless, S.J., Kozhushko, A.A., 1999. Failure wave effects in hyper-velocity penetration. Int. J. Imp. Eng. 23, 995–1001.